AGToLightM: A Deep Learning Model for 60-Minute Thunderstorm Probability Nowcasting by Fusing FY-4B Satellite Infrared and Ground-Based Lightning Data

Junjie Yan , Jun Liu , Jianhua Qu , Runjia Li *

Posted Date: 25 March 2026

doi: 10.20944/preprints202603.2018.v1

Keywords: AGToLightM; FY-4B/AGRI; nowcasting; case analysis

 doi:10.20944/preprints202603.2018.v1

Article

AGToLightM: A Deep Learning Model for 60-Minute Thunderstorm Probability Nowcasting by Fusing FY-4B Satellite Infrared and Ground-Based Lightning Data

Junjie Yan [1,2], Jun Liu [1,2], Jianhua Qu [3] and Runjia Li [1,2,*]

[1] Key Laboratory of Intelligent Meteorological Observation Technology, China Meteorological Administration, Beijing 100081, China

[2] China Huayun Meteorological Technology Group Co., Ltd., Beijing 100081, China

[3] Beijing Huayun Shinetek Science and Technology Co. Ltd., Beijing 100081, China

* Correspondence: Lirunjia2022@163.com

Abstract

Lightning activity reflects the occurrence of severe convective events and is the most prominent physical feature of thunderstorms. This study develops the AGToLightM model to predict the probability of thunderstorm occurrence within the next 60 minutes by combining FY-4B/AGRI multi-channel infrared brightness temperature data (with a temporal resolution of 15 minutes and a spatial resolution of 4 km) with ground-based lightning observations. Based on the characteristics of lightning events, the model incorporates a Convolutional Block Attention Mechanism (CBAM) to enhance the extraction of critical spatial and channel features at cloud tops. An adaptive weighted loss function is employed to address the class imbalance caused by sparse positive lightning samples. Three study zones in China—North China, East China, and South China—were selected, with summer 2025 data used for model training and validation. Results indicate that AGToLightM effectively captures the spatial distribution and evolution of thunderstorms, achieving a maximum Critical Success Index (CSI) of 0.327. In case studies, regions with forecast probabilities exceeding 60% show high spatial consistency in areas with radar echoes above 50 dBZ. These findings demonstrate the effectiveness of the AGToLightM model in integrating multi-source meteorological data for severe convective nowcasting and provide technical guidance for improving the reliability of short-term thunderstorm predictions.

Keywords: AGToLightM; FY-4B/AGRI; nowcasting; case analysis

1. Introduction

Thunderstorms are intense convective weather systems that generate lightning. Lightning activity, particularly the total lightning flash rate (comprising intra-cloud and cloud-to-ground lightning), reflects the occurrence of deeply electrified convection [1]. Various studies have demonstrated that in single-cell, multicellular storms [2–7], and tropical cyclones [8,9], total lightning activity exhibits strong correlations with indicators such as updraft intensity and precipitation. Consequently, lightning density mirrors storm development and serves as a critical meteorological variable for identifying severe convective weather. Therefore, lightning data are essential for locating deep convective systems [10], providing significant practical value for thunderstorm identification and tracking.

Thunderstorm warning research originated earlier in international contexts. Countries such as the United States and Europe have invested substantial resources in lightning monitoring and early warning systems, establishing comprehensive lightning monitoring networks and warning systems.

 doi:10.20944/preprints202603.2018.v1

The National Lightning Detection Network (NLDN) in the United States monitors lightning activity nationwide in real time. By integrating meteorological satellite and radar data with numerical modeling, statistical methods, and extrapolation analysis [11], it provides thunderstorm warnings. India has established a multidimensional monitoring network comprising 558 meteorological stations, 25 Doppler radars, INSAT series satellites, and 48 lightning sensors. The forecast employs extrapolation methods, explicit storm models, and a human-machine integrated expert system to enhance forecast accuracy [12]. In recent years, research efforts worldwide have increasingly focused on integrating machine learning with physical mechanisms. For instance, algorithms such as random forests and artificial neural networks are being employed to fuse multi-source observational data and optimize thunderstorm warning services. For example, Yousefnia et al. developed a machine learning-based lightning activity recognition model (SALAMA 1D) that integrates convective-permitted numerical weather prediction vertical profiles for thunderstorm forecasting and evaluates model performance [13].

Since the 1990s, China has routinely utilized sounding data to calculate and analyze conditions conducive to thunderstorm development, enabling thunderstorm warnings. For instance, Zhang et al. investigated how lightning activity within different cloud systems and characteristics related to convective precipitation influence thunderstorm activity [14]. Numerical forecasting techniques for severe convective weather such as thunderstorms have been continuously advancing [15]. Subsequently, real-time monitoring and nowcasting technologies, including thunderstorm cell identification and tracking, have gradually developed. With the rapid advancement of artificial intelligence and big data technologies, China's lightning forecasting is progressively transitioning from traditional empirical statistics and numerical modeling toward intelligent, data-driven approaches. Intelligent methods such as machine learning and deep learning are being widely applied to lightning nowcasting. For instance, Song et al. proposed a machine learning-based lightning nowcasting model that significantly enhances forecasting performance by incorporating aerosol information and enhanced satellite observation data [16].

Each thunderstorm exhibits unique lightning characteristics, with lightning activity reaching specific maxima and minima throughout the storm lifecycle [5,17]. Quantifying variations in lightning activity enables analysis of the developmental processes within thunderstorm cell time series. Bourscheidt et al. demonstrated the potential of lightning for near-term precipitation forecasting using GOES GLM lightning observations (with a coefficient of determination of approximately 0.6), though limitations exist in accurately predicting high-intensity rainfall rates and accumulation [18].Felix et al. utilized various products from the Geostationary Lightning Mapper (GLM) and Advanced Baseline Imager (ABI) aboard the GOES satellite to analyze cloud characteristics of thunderstorms. They classified storms based on whether they produced GEO LJ, GEO LD, and severe weather [19]. Thiel et al. distinguished convective precipitation from layered precipitation by analyzing the size and frequency of GLM flashes [20]. Kelly et al. integrated GLM real-time lightning data with radar vertically integrated liquid water (VIL) content to develop the VILFRD quantitative metric, enabling automated algorithms for dynamic thunderstorm identification and trajectory tracking [21]. Chinchay et al. demonstrated that the ABI instrument aboard GOES-R provides valuable information for short-term forecasting of thunderstorms [22,23]. In recent years, China's ground-based lightning detection technology have advanced rapidly, establishing a multi-station, full-lightning three-dimensional real-time positioning network. In 2020, China's meteorological operational network underwent a comprehensive upgrade. Adopting a “floating-level pulse recognition + dual-frequency cross-verification” algorithm, it effectively suppresses urban electromagnetic noise, reducing the height error of long-baseline 3D measurements from 500 m to approximately 200 m. The system also features real-time waveform output and type identification capabilities. Ground-based lightning data has found applications in thunderstorm monitoring and early warning systems, particularly in data assimilation forecasting and thunderstorm phenomenon analysis.The Fengyun-4B satellite (FY-4B) is the second satellite in China's new generation of geostationary meteorological satellites, successfully launched on June 3,

 doi:10.20944/preprints202603.2018.v1

2021 [24,25]. Its onboard AGRI instrument provides observation data with 15-minute resolution, achieving notable application results in weather monitoring, early warning, and forecasting. For instance, X. Zhang [26] and Zhang et al. utilized FY-4B data to identify and extract convective clouds [27]. Wu et al. analyzed cloud thermal characteristics using FY-4 imager data and ERA5 reanalysis data, enabling hail monitoring [28]. Ren et al. combined FY-4A multi-channel convective composite products with lightning imager data to analyze their characteristics during thunderstorms, demonstrating the composite products' outstanding performance in convective storm clouds with strong updrafts [29].

The present study proposes a nowcasting method to predict the probability of thunderstorm occurrence within a 60-minute lead time. By leveraging the radiative characteristics of FY-4B/AGRI infrared channels across various cloud phases, this study establishes a quantitative relationship between these spectral signatures and the spatial distribution of lightning. The thunderstorm forecasting model AGToLightM is constructed to achieve quantitative forecasting of thunderstorm occurrence probability. This paper primarily describes the construction process of the AGToLightM model, the loss function selection strategy, and validation results across different geographic zones. It analyzes the influence of each input feature channel on thunderstorm forecasting. Furthermore, using typical severe convective cases, the model's applicability in short-term thunderstorm forecasting through the fusion of multi-source meteorological data is evaluated by comparing radar echo intensity distributions.

2. Study Area and Data

2.1. Study Area

This study selected three zones in China—East China, North China, and South China—as the research areas, as detailed in Table 1. Zone I: Southeastern coastal China (111.98°E–119.98°E, 26.02°N–34.02°N), covering most of Zhejiang, northeastern Jiangxi, eastern Hunan, northwestern Fujian, and parts of southern Anhui and Hubei. This zone, influenced by the East Asian monsoon and complex topography, is one of China's high-frequency lightning activity zones [30]. Its surface temperature, humidity, and atmospheric instability configuration in the lower and middle layers are conducive to the development of strong convection [31]. Zone II: Beijing, Hebei, and surrounding areas (112.02°E–120.02°E, 34.02°N–42.02°N) features a temperate monsoon climate. From June to September, it experiences frequent convective activity influenced by warm, moist southeasterly maritime airflows [32]. Thunderstorms predominantly occur near bodies of water and mountain ranges. During specific periods, these features provide conditions for thermal or dynamic lifting, coupled with ample moisture supply, which is conducive to intra-cloud electrification and thunderstorm formation [33]. Zone III: Southern South China and Northern South China Sea Coastal Areas (105°E-113°E, 18.02°N-26.02°N). Under the combined influence of the tropical monsoon and marine air masses, this zone exhibits active thunderstorm activity [34], demonstrating pronounced spatiotemporal clustering characteristics. These three zones respectively represent China's subtropical high-frequency lightning zone, temperate low-to-medium frequency lightning zone, and tropical coastal lightning zone, covering distinct weather environments and providing a foundation for subsequent model validation. Specific distribution details are shown in Figure 1 (national lightning observation distribution diagram for July 11, 2025).

 doi:10.20944/preprints202603.2018.v1

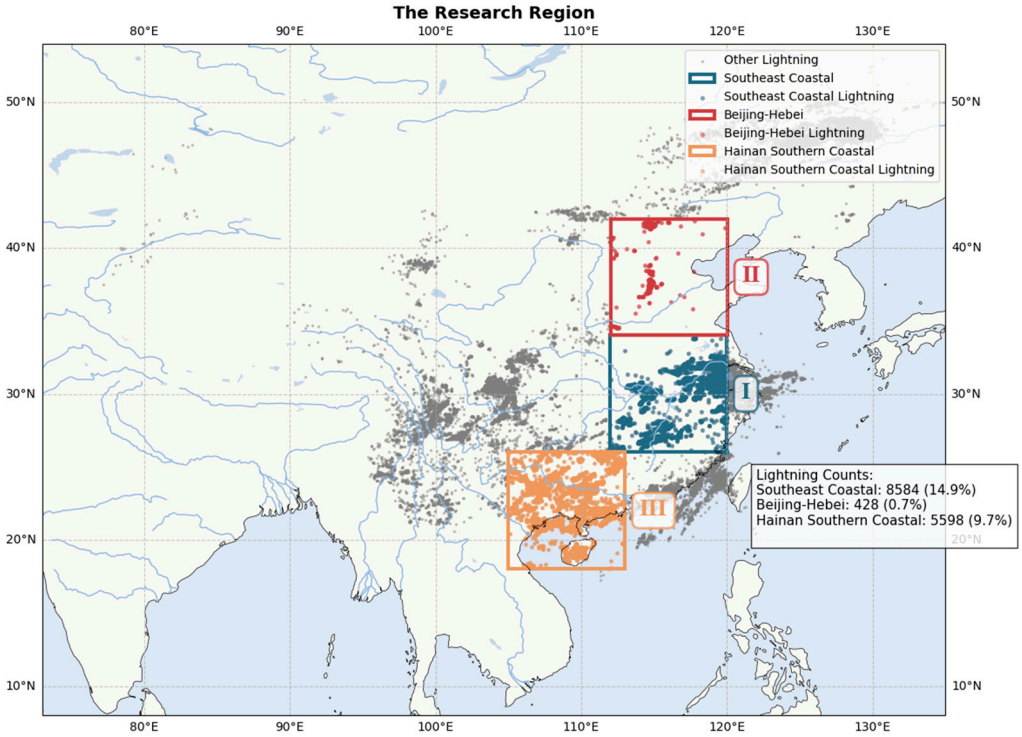

Figure 1. Spatial distribution of national lightning observations on July 11, 2025 (UTC). The map illustrates the lightning density and occurrence across the selected study zones (East, North, and South China) used for model validation.

Table 1. Geographic coordinates and regional classifications of the three selected study areas in China.

Zone ID	Zone Name	Longitude Range
I	East China Region	111.98°E-119.98°E
II	North China Region	112.02°E–120.02°E
III	South China Region	105°E–113°E

2.2. Ground-Based Lightning Detection Data

The ground-based lightning observation data used in this paper are sourced from the Tianqing System of the China Meteorological Administration. They comprise lightning data recorded by 419 observation sites using a combination of ADTD and DDW1 equipment [35,36], documenting the occurrence time, latitude and longitude, and lightning category of each strike.

In the late 2000s, the China Meteorological Administration began constructing a national ground-based lightning detection network. The ADTD lightning detection sensors deployed in this network can locate cloud-to-ground lightning within the 1 kHz to 450 kHz frequency band. With a detection range of approximately 300 km per ADTD sensor [37]. Lightning location is achieved by combining magnetic direction finders with time-of-arrival methods. Multiple substations are networked (with baseline distances of 100–200 km), forming a nationwide coverage network [38].In recent years, the ADTD lightning detection system has undergone upgrades, gradually incorporating DDW1 lightning detectors [39], enhancing its capability to detect intra-cloud lightning [38]. In 2022, Zhang Yang et al. [39] evaluated the ADTD system's performance using artificially triggered lightning. Detection efficiencies reached 100% for cloud-to-ground lightning and approximately 63% for intra-cloud lightning, with an average positioning error of 464 meters for intra-cloud lightning events.

Ground-based lightning detection data provides the detected lightning's latitude, longitude, and time information, serving as labeled data for thunderstorm models.

 doi:10.20944/preprints202603.2018.v1

2.3. FY-4B/AGRI Data

The Fengyun-4B satellite (FY-4B) is China's first operational next-generation geostationary meteorological satellite, successfully launched on June 3, 2021, and positioned at 133°E over the equator. The data utilized in this study originate from the Advanced Geosynchronous Radiation Imager (AGRI) aboard FY-4B. The AGRI instrument is equipped with 15 spectral channels, AGRI achieves spatial resolutions ranging from 0.5 km (visible light) to 4 km (longwave infrared) and performs full-disk scans at 15-minute intervals. This research primarily employs FY-4B AGRI infrared band data, with parameters detailed in Table 2.

Table 2. Specifications and meteorological applications of the FY-4B/AGRI infrared channels utilized in the AGToLightM model.

Band	Center Wave Length	Bandwidth	SR	Applications
8	3.75μm	3.50-4.0μm (Low)	4km	Low-albedo targets and surface features
9	6.25μm	5.80-6.70μm	4km	Upper-level moisture
10	6.95μm	6.75-7.15μm	4km	Mid-level moisture
11	7.42μm	7.24-7.60μm	4km	Lower-level moisture
12	8.55μm	8.3-8.8μm	4km	Clouds
13	10.80μm	10.30-11.30μm	4km	Clouds, surface temperature, etc.
14	12.00μm	11.50-12.50μm	4km	Clouds, total water vapor, surface temperature
15	13.3μm	13.00-13.60μm	4km	Clouds, water vapor

2.4. Radar Reflectivity Data

The radar composite reflectivity data used in this paper is sourced from the Tianqing System of the China Meteorological Administration. It is a radar network product that includes nationwide composite reflectivity data with a spatial resolution of 1 km and a temporal resolution of 6 minutes.

3. Methods

3.1. Data Preprocessing

Lightning data, serving as structured labels for the model, undergoes spatial resampling processing first. Considering the resolution of the AGRI infrared channel from Fengyun-4B satellite used in model development, this study grids and resamples the lightning data to a 4 km resolution. Lightning location data from the China Meteorological Administration's operational lightning detection system originates from two ground-based lightning observation devices: ADTD and DDW1. Both systems cover observation ranges reaching hundreds of kilometers. Raw data undergoes lightning location processing using methods such as time-based localization, achieving an accuracy of approximately 500m [40]. The arithmetic mean, geometric mean, median, and standard deviation of the planar positioning accuracy for the DDW1 lightning detection device are all less than 500 m [35]. Spatial resampling with a target spatial resolution of 4 km ensures the accuracy of spatial matching for labeled data. B. Lynn et al. used the Lightning Potential Index (LPI) to confirm that this resolution can effectively reflect the overall distribution characteristics of lightning [41]. Lightning data undergoes both temporal and spatial matching during resampling. Temporally, all lightning events within a 60-minute window are synchronized with AGRI observation times. For these events, lightning strike zones and density are calculated based on latitude and longitude. Using a 60-minute sliding window, lightning locations are computed for each grid cell. Lightning strike zones are represented as binary data.

The FY-4B/AGRI data encompass multiple infrared channels ranging from 3.75 μm to 13.30 μm, which are extensively utilized in monitoring and forecasting severe convective weather. This study

 doi:10.20944/preprints202603.2018.v1

employs all infrared channels from AGRI as feature factors for the model. To enhance the detection of pre-thunderstorm characteristics, channel differences and channel-time differences are incorporated as supplementary features, as shown in Table 3.

Table 3. Summary of the multi-dimensional input features in the AGToLightM model, including raw AGRI infrared brightness temperatures (BT), inter-channel brightness temperature differences (BTDs), and their respective temporal variations (TBDTs). These features characterize the static thermodynamic state and the dynamic evolutionary processes of convective clouds.

Num	Channel	Description
1	BT(IR3.75)	T0 single-channel brightness temperature, showing low clouds and cloud-top temperature
2	BT(WV6.25)	T0 single-channel brightness temperature, showing upper-level water vapor
3	BT(WV6.95)	T0 single-channel brightness temperature, showing mid-level water vapor
4	BT(WV7.42)	T0 single-channel brightness temperature, showing lower-level water vapor
5	BT(IR8.55)	T0 single-channel brightness temperature, showing clouds
6	BT(IR10.80)	T0 single-channel brightness temperature, showing cloud-top temperature
7	BT(IR12.00)	Single-channel brightness temperature at T0 time, indicating cloud top temperature
8	BT(IR13.30)	Single-channel brightness temperature at T0 time, indicating clouds and water vapor
9	BTD(6.25–7.42)	Brightness temperature difference between channels at T0 time, indicating upper/lower layer water vapor difference
10	BTD(10.80–8.55)	Brightness temperature difference between channels at T0 time, indicating cloud phase (ice clouds/water clouds) difference
11	BTD(12.00–10.80)	Brightness temperature difference between channels at T0 time, indicating cloud phase (ice clouds/water clouds) difference
12	TBDT(10.80)	Brightness temperature difference between (T0 - 15min) and T0, indicating cloud top temperature change
13	TBDT(12.00)	Brightness temperature difference between (T0 - 15min) and T0, indicating cloud top temperature change
14	TBDT(10.80–8.55)	Brightness temperature difference between (T0 - 15min) and T0, indicating cloud top temperature change
15	TBDT(12.00–10.80)	Brightness temperature difference between (T0 - 15min) and T0, indicating cloud top temperature change

Strong convective cloud clusters (such as thunderstorm cells) exhibit distinct characteristics, containing significantly more intra-cloud ice particles than other cloud systems and being accompanied by intense moisture transport. Both the 6.25 μm and 7.42 μm channels are moisture absorption bands, detecting upper-level and lower-level moisture respectively. Their difference directly reflects the degree of anomaly in the atmospheric vertical moisture gradient [42]. Steeper gradients indicate greater convective potential and serve as precursors to thunderstorm development. The 10.80 μm and 12.00 μm channels exhibit differing sensitivities to liquid water and ice particles: 12.00 μm shows stronger scattering and absorption from large ice particles, while 10.80 μm provides more stable liquid water responses. The differential between 12.00 μm and 10.8 μm can identify deep convective clouds, with its magnitude dependent on cloud optical thickness, liquid water content, chemical composition, and particle size distribution [43].The 8.55 μm channel is sensitive to small ice particles, and its differential with the 10.80 μm channel reflects cloud phase and particle size. Small ice particle formation in strong convective cloud tops precedes “cold cloud tops” (BT10.8 decrease). Positive values in the 8.55 μm versus 10.80 μm difference may appear 30–60 minutes earlier, enabling advance convective warnings [44,45]. Based on this, three infrared channel differences were

 doi:10.20944/preprints202603.2018.v1

incorporated into the model construction: 6.25 μm versus 7.42 μm, 12.00 μm versus 10.80 μm, and 8.55 μm versus 11μm.

Meickalski et al. research [46] demonstrated that differences in infrared channel values already exist before immature cumulonimbus clouds develop into convective storms. Establishing the relationship between these changes prior to initial convective development can provide valuable information for short-term forecasting algorithms. Based on this, the model incorporates the differences between the previous and current observations for three pairs of factors: 6.25 μm and 7.42 μm, 12.00 μm and 10.80 μm, and 8.55 μm and 10.80 μm.

3.2. Model Design

The AGToLightM model employs a U-Net architecture with encoder and decoder components [47]. By establishing relationships between multi-source features from the FY-4B/AGRI and ground-based lightning observations, the model calculates the probability of thunderstorm occurrence for a 60-minute lead time.

The U-Net model effectively extracts local spatial features and fine-scale patterns through convolutional neural networks (CNNs) [48]. It possesses the capability to process multiple feature factors, fully uncovering the multidimensional information linking various factors to thunderstorm activity [49]. By precisely capturing lightning-associated small-scale information—such as cloud-top glaciation and local brightness temperature gradients—This architecture can achieve pixel-level lightning probability prediction, breaking through the limitations of traditional regional-level forecasting [22]. Furthermore, its encoder-decoder architecture enables high-precision image semantic segmentation even with limited training data [50]. The U-Net model possesses end-to-end learning capabilities [50], eliminating the need for manually designed features. It autonomously extracts lightning-associated patterns consistent with thunderstorm weather elements from satellite observation data, reducing reliance on human expertise [51].

In the AGToLightM architecture developed in this study, the encoder path incorporates four subsampling stages: Initially, the DoubleConv module (comprising two consecutive 3 × 3 convolutions, each with batch normalization and ReLU activation) expands the 9 input channels to 64 channels. Subsequently, four downsampling modules progressively increase the channel count to 1024 while simultaneously reducing the feature map size from 200 × 200 to 12 × 12, extracting multi-scale spatial features. The decoder path employs four upsampling modules using 2 × 2 transposed convolutions to restore the abstract features extracted by the downsampling path into high-resolution outputs. These are then fused with the encoder's multi-scale features through skip connections. At the network's end, a 1 × 1 convolution maps the 64-channel features into a single-channel lightning probability output, enabling pixel-level lightning probability prediction.The structure and training method of AGToLightM are shown in Figure 2.

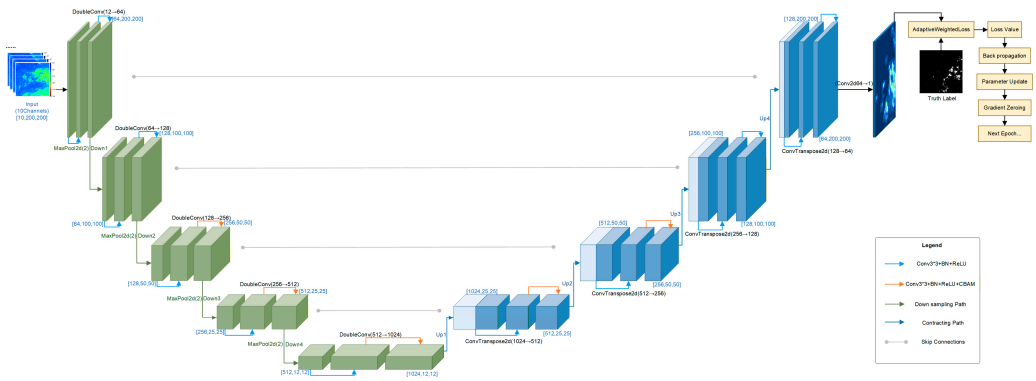

Figure 2. Structure and Training Method of AGToLightM.

 doi:10.20944/preprints202603.2018.v1

CBAM is an attention module integrated into a feedforward convolutional neural network, comprising both channel attention and spatial attention components, as shown in Figure 3 For the AGToLightM model, the channel attention mechanism enables adaptive computation of channel importance, amplifying weights for channels highly correlated with thunderstorm events while suppressing noise interference from irrelevant channels. The spatial attention mechanism aggregates global average responses and local maximum responses across feature maps, focusing on critical regions prone to thunderstorms (e.g., the core region of strong convection). Within the AGToLightM model, CBAM achieves efficient multi-view feature collaboration through a two-step fusion process: First, the channel attention mechanism dynamically assigns view weights based on feature requirements at different stages of thunderstorm development. Second, the spatial attention mechanism further aggregates spatially correlated information from multiple views on the channel-weighted feature maps, thereby locating the core thunderstorm region and improving model performance.

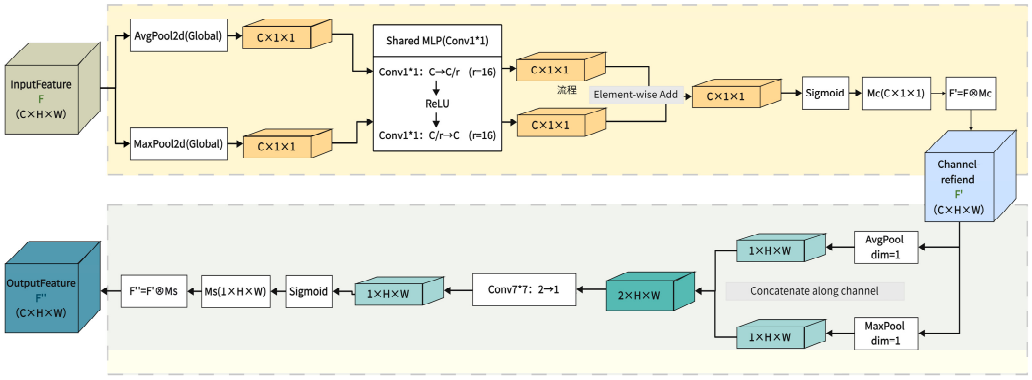

Figure 3. Schematic of the Convolutional Block Attention Module (CBAM) integrated into the AGToLightM architecture.

In the shallow layers of the model, feature factors possess high spatial resolution and abundant structural details (e.g., edge contours and local textures of thunderstorm clouds), but their semantic representation is limited, making it difficult to distinguish specific meteorological categories. As the downsampling depth increases, spatial details gradually degrade, while semantic information becomes more prominent, allowing the model to capture abstract features directly related to thunderstorm formation. Based on this evolution pattern, the AGToLightM model maintains the basic U-Net architecture in its shallow layers while embedding CBAM into the deeper network. This design ensures the preservation of high-fidelity spatial details in the shallow layers while leveraging the attention mechanism to adaptively filter key features and spatial information in the deep layers, thereby strengthening the response to critical meteorological signatures.

To address the challenge of severe positive-negative sample imbalance and scarcity of positive samples in thunderstorm forecasting, this study introduces pixel-level underestimation penalty weights (Equation 1) and batch-level false-negative rate adaptive weights (Equations 2 and 3) on top of Focal Loss ($\alpha = 0.95$, $\gamma = 1.5$) to construct a comprehensive adaptive weight (Equation 4). Combined with Focal Loss, this forms the final loss function (Equation 5). This approach balances samples while focusing on challenging cases, intensifies penalties for missed detections, and dynamically tracks missed detection trends during training. This enables adaptive optimization of the model's predictive capability for rare thunderstorm events. Furthermore, this study introduces an adaptive weighted loss dynamic adjustment strategy based on the CBAM attention mechanism. By integrating CBAM's spatial and channel attention scores, the model dynamically adjusts loss weights for each sample in real-time, particularly focusing attention allocation toward positive sample regions. When attention to positive regions is low, the adaptive weight in the loss function automatically increases to enhance the model's focus on these rare events. Similarly, when overall attention is low, the weights in the loss function are appropriately increased to ensure the model focuses more on challenging-to-predict

 doi:10.20944/preprints202603.2018.v1

regions. This aims to enhance the model's prediction accuracy for sparse thunderstorm events and improve its sensitivity to key meteorological features.

$$W_{pixel} = 1 + \lambda \cdot \max(0, y - \hat{y}) \tag{1}$$

$$FN_{EMA}^{(t)} = \beta \cdot FN_{EMA}^{(t-1)} + (1-\beta) \cdot FN_{batch}^{(t)} \tag{2}$$

$$W_{global} = \min(\max(1 + FN_{EMA}, W_{\min}), W_{\max}) \tag{3}$$

$$W_{final} = \min(\max(W_{pixel} \cdot W_{global}, W_{\min}), W_{\max}) \tag{4}$$

$$L_{adaptive} = \frac{1}{N} \sum_{i=1}^{N} W_{final}^{(i)} \cdot FocalLoss(p^{(i)}, y^{(i)}) \tag{5}$$

3.3. Model Application and Evaluation Indicators

In this study, data collected from June 1 to August 20, 2025, were utilized for model construction. To minimize the interference of non-convective samples on performance evaluation, the dataset was filtered based on lightning activity intensity thresholds, effectively excluding periods with no lightning events. For each of the three geographical regions, representative samples exhibiting distinct thunderstorm characteristics were selected for testing and validation. The detailed distribution of the dataset is presented in Table 4.

To quantitatively evaluate the model's performance, four key metrics were selected: Probability of Detection (POD), Precision, F1-score, and the Critical Success Index (CSI). These metrics were calculated by comparing the predicted one-hour thunderstorm probabilities with ground-based lightning observations.

Table 4. Overview of the experimental dataset across three geographical zones (East, North, and South China). The table specifies the number of samples allocated for training, testing, and validation, focusing on periods with active lightning events during the summer of 2025.

Zone ID	Zone Name	Training Data	Test Data	Validation Data
I	East China Region	4124	1031	95
II	North China Region	4680	1170	95
III	South China Region	4979	1245	95

The POD measures a model's ability to capture actual lightning events, calculated as the proportion of correctly forecasted lightning samples (TP) out of all actual lightning samples (TP + FN). Precision reflects the proportion of correctly forecasted events among all events forecasted as "thunderstorm present." It is calculated as the ratio of correctly forecasted thunderstorm events (TP) to all events forecasted as "thunderstorm present" (FP + TP). The F1-score is the harmonic mean of precision and POD, used to comprehensively evaluate a model's balanced performance in identifying positive class samples. The Critical Success Index (CSI) measures the model's overall effectiveness in lightning prediction, calculated as the ratio of correctly forecasted lightning samples (TP) to all samples requiring attention (TP + FN + FP). A higher POD indicates fewer missed detections [22,52]. Higher precision signifies greater forecast accuracy, meaning fewer false positives. A higher F1 score indicates the model better balances accuracy and comprehensiveness [52]. A higher CSI value represents superior overall forecasting performance [22,52].

$$POD = \frac{TP}{TP + FN} \tag{6}$$

$$Precision = \frac{FP}{TP + FP} \tag{7}$$

 doi:10.20944/preprints202603.2018.v1

$$F1\text{-}score = \frac{2 \times TP}{2 \times TP + FN + TP} \tag{8}$$

$$CSI = \frac{TP}{TP + FN + FP} \tag{9}$$

4. Result

4.1. Comparative experiment

To analyze the application effects of integrating the CBAM attention mechanism with the loss function, this study conducted a series of comparative experiments based on identical datasets, taking East China as a case study. The experiments include: (1) using only the Focal Loss function with fixed parameters; (2) incorporating the CBAM attention mechanism and an adaptive weighted loss strategy; (3) employing a loss function dynamically tuned by combining CBAM with the adaptive weighted loss mechanism; and (4) introducing a threshold penalty mechanism based on the third experimental group.

4.1.1. Focal Loss Loss Function with Fixed Parameters

In this experimental group, Focal Loss with fixed parameters (α = 0.95, γ = 1.5) was employed during training to address the scarcity of positive lightning samples. The objective was to enhance the model's focus on positive samples; however, neither the CBAM attention mechanism nor any other loss function enhancement mechanisms were incorporated.

Experimental results indicate that Focal Loss can alleviate the imbalance between positive and negative samples to a certain extent. However, when handling rare events, the model still suffers from an overall low forecast probability; the forecast probabilities for regions where thunderstorms occurred are concentrated between 20% and 40%, with only a few areas reaching a forecast probability of 50% or higher. Furthermore, the model fails to pay sufficient attention to hard-to-predict regions, such as the edges or smaller areas of lightning activity. Figure 4 displays the forecast results obtained by training the model solely with the Focal Loss function and applying it to typical time steps in East China. The forecast results are presented in the form of a probability heat map, where the color transitions from deep blue to deep red, representing the thunderstorm occurrence probability increasing from 0 to 1.0 (see the vertical color bar on the right for details). The colored solid lines in the figure are probability contours, which respectively mark the probability threshold boundaries from 20% to 60%, used to visually define the coverage of the forecast field. The bright yellow pixels scattered throughout the figure represent the ground truth data from lightning locators at that time step, used to verify the degree of coincidence between the forecast center and the actual thunderstorm positions.

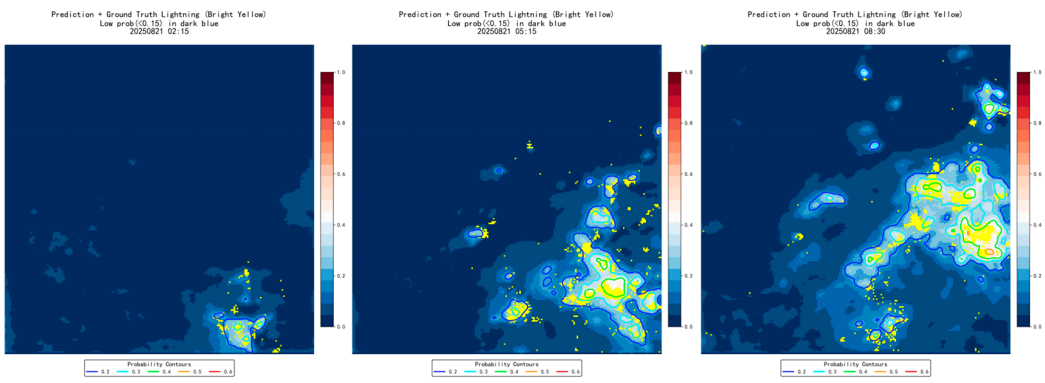

Figure 4. Forecasting results of the model using only the Focal Loss function for a representative time period in East China in 20250821 (UTC).(The background color represents the lightning occurrence probability output by

 doi:10.20944/preprints202603.2018.v1

the model, with the color bar ranging from 0.0 to 1.0; deep blue indicates low forecast probability, while deep red indicates high forecast probability. The colored contours, transitioning from blue to red, sequentially represent the probability threshold boundaries of 0.2 to 0.6. Bright yellow pixels denote the ground truth of lightning strikes for the corresponding time steps.).

4.1.2. Introducing the CBAM and Adaptive Weighted Loss Strategy

In this experimental group, the CBAM attention mechanism was added to the deep layers of the model based on the original Focal Loss (α = 0.95, γ = 1.5) function, enabling the model to focus on important feature channels and regions related to thunderstorm formation. Additionally, an adaptive weighted loss strategy was adopted to dynamically adjust the weight of each sample according to the model's learning process; for underestimated positive samples, the loss weight was increased to strengthen the penalty for false negatives. Compared to the model applying only the Focal Loss function, the model trained in this experimental group increased the forecast probability for thunderstorm-active areas to between 30% and 60%, and the extent of areas with forecast probabilities of 50% or higher significantly expanded, enhancing the predictive capability for rare events (localized thunderstorm regions).

Figure 5 shows the forecast results of the model trained by incorporating the CBAM attention mechanism and the adaptive weighted loss strategy, applied to typical time steps in East China. For the typical time steps especially at 05:15 and 08:30 on August 21, 2025, the high-probability regions of the improved model (areas with a forecast probability >50%) are in high spatial agreement with the observed dense lightning clusters, enabling a more precise capture of the evolutionary characteristics of localized thunderstorms.

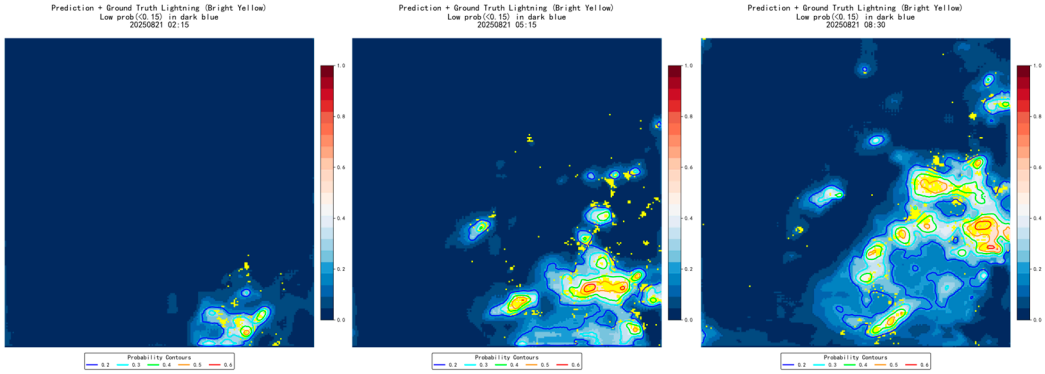

Figure 5. Forecasting results of the model incorporating the CBAM mechanism and the adaptive weighting strategy for a representative time period in East China in 20250821 (UTC).

4.1.3. Loss Function Dynamically Optimized via CBAM and Adaptive Weighting

This study incorporates an adaptive weighted loss dynamic adjustment strategy based on CBAM attention scores, which dynamically adjusts the λ value in the loss function according to the CBAM attention scores. When the attention response in a positive sample region is low, the λ value is increased to strengthen the penalty for that area, forcing the model to focus on hard-to-predict regions with ambiguous features and enhancing the model's predictive performance for thunderstorm events.

Figure 6 shows the forecast results of the model trained with the loss function dynamically tuned by combining CBAM and the adaptive weighted loss mechanism, applied to typical time steps in East China. Comparing Figure 6 with Figure 5 reveals that the dynamic tuning mechanism based on CBAM scores achieves a significant improvement in forecast efficiency. The spatial alignment precision between the high-probability regions predicted by the model and the areas where lightning actually occurred is further improved. The forecasts for time steps such as 02:15, 05:15, and 08:30 are

 doi:10.20944/preprints202603.2018.v1

all more precise, effectively reducing false alarms in non-thunderstorm areas while simultaneously reducing missed detections.

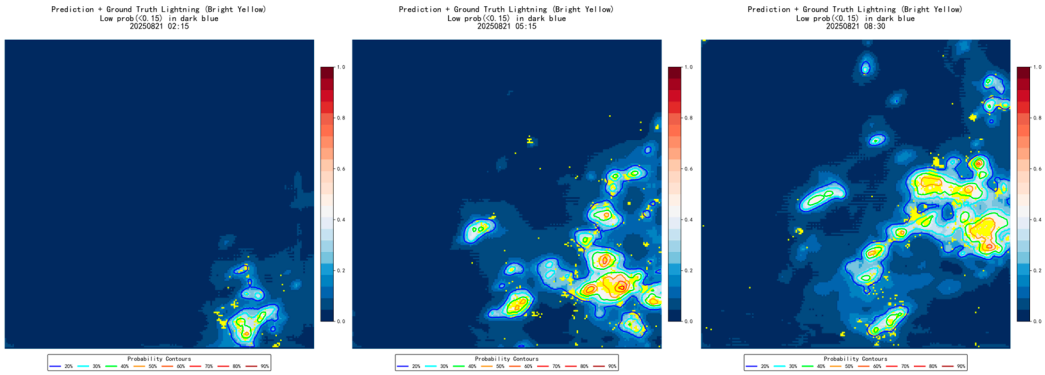

Figure 6. Forecasting results of the model utilizing the dynamically optimized loss function integrated with CBAM attention scores for a representative time period in East China in 20250821 (UTC).

4.1.4. Addition of Threshold Penalties

To further constrain the trade-off between missed detections and false alarms, this experimental group added threshold constraints based on the current loss function. Specifically, a penalty is imposed on non-lightning samples when the predicted probability exceeds the negative sample threshold (20%), and a penalty is applied to lightning samples when the predicted probability falls below the positive sample threshold (50%). The purpose is to suppress false alarms and reduce missed detections, enabling the model to output forecast results with higher discriminability.

Experimental results for Figure 7 indicate that while this constraint mechanism significantly improves the hit rate, the false alarm rate also increases substantially. By applying penalties to positive samples, the model enhances the forecast probability in "lightning-active" regions, leading to an increase in areas with probabilities of 50% or higher, which almost completely cover the ground truth areas of lightning observations. However, a large number of non-lightning regions are also predicted with high thunderstorm occurrence probabilities. The primary reason is that the strong positive sample penalty causes the overall probability of the model results to shift upward, leading to many non-lightning areas being misjudged as lightning-active regions and increasing false positives. This phenomenon is further exacerbated by the spatial smoothing effect caused by convolutional operations and the asymmetry of the penalties applied to positive and negative samples.

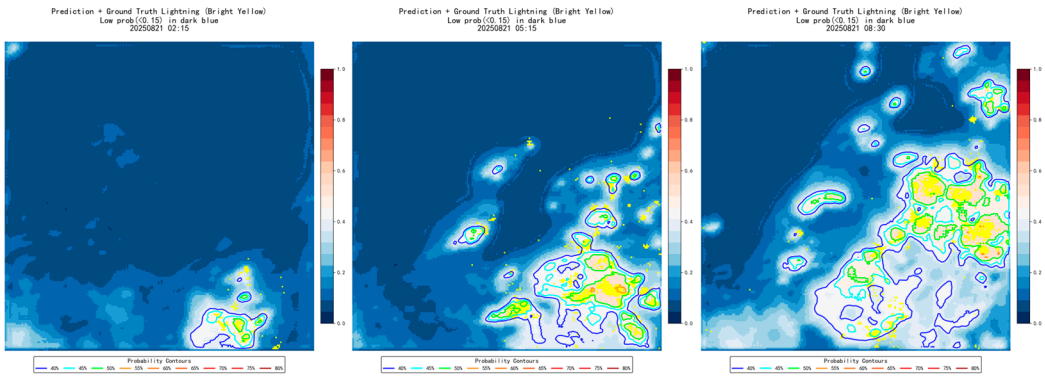

Figure 7. Forecasting results of the model after incorporating the threshold penalty mechanism for a representative case in East China in 20250821 (UTC).

4.2. Model Performance

 doi:10.20944/preprints202603.2018.v1

Following the training scheme proposed in Chapter 3, the AGToLightM model was independently validated across three regional test sets. Representative cases were selected for analysis: Zone I (East China) on August 25, 2025 (UTC); Zone II (North China) on August 21, 2025 (UTC); and Zone III (South China) on August 27, 2025 (UTC).

As a probabilistic forecasting model, AGToLightM outputs the likelihood of thunderstorm occurrences rather than deterministic categories. Therefore, it is essential to examine the model's performance under various decision thresholds. This approach allows for a more nuanced understanding of the trade-off between sensitivity and specificity, thereby enhancing the comprehensiveness of the performance evaluation. Table 5 summarizes the POD and Precision of AGToLightM at typical probability thresholds (20%, 30%, ... 60% and above) for each study area. The results exhibit a characteristic inverse relationship between the hit rate (POD) and precision as the threshold increases. To further determine the optimal operating point that balances these competing metrics, the Critical Success Index (CSI) will be statistically analyzed in the following section.

Table 5. Performance metrics (POD and Precision) of the AGToLightM model across three study regions at different probability thresholds.

Test Data	Probability threshold	20%	30%	40%	50%	60%+
20250825 Zone I	POD (%)	93.0	85.2	73.9	53.4	22.9
	Precision (%)	5.1	7.8	11.1	17.8	32.8
20250821 Zone II	POD (%)	84.8	73.5	56.6	37.2	0
	Precision (%)	12.3	15.8	20.6	28.8	0
20250827 Zone III	POD (%)	89.7	74.7	46.3	11.8	0
	Precision (%)	5.4	7.2	11.8	19.4	0

The model CSI performance chart evaluates the model's performance at different probability thresholds. As shown in Figure 8, the CSI performance plots for Zones I, II, and III are presented from left to right. The horizontal axis represents Precision, while the vertical axis denotes POD. The black curve traces the model's performance trajectory across different probability thresholds, with key threshold points marked (10%, 15%, 20%, 30%, 50%, 70%, 90%). The yellow shaded regions correspond to different CSI values, with darker shades indicating higher CSI. Curves closer to the upper-right corner (high POD, high Precision) and passing through darker shaded areas indicate higher CSI at that threshold. This plot identifies the optimal probability threshold that maximizes CSI and visually illustrates the performance trade-offs at different thresholds. Table 6 shows the best critical success index (CSI) values for the AGToLightM model across three test datasets, along with their corresponding probability thresholds and precision metrics. Analysis of the charts reveals that Zone I (East China) exhibits superior CSI curve characteristics and optimal CSI values compared to the other two regions. This indicates a relatively balanced performance in both false positives and false negatives for thunderstorms. The optimal CSI corresponds to a probability threshold of 46%, slightly lower than that of North China. Furthermore, the chart reveals that the model yields zero forecasts in high-probability zones (probability ≥ 60%), suggesting a conservative approach to thunderstorm prediction. Zone II (North China) exhibits a higher optimal probability threshold than the other two regions. The model demonstrates a tendency toward higher probability forecasts, achieving relatively high hit rates across various probability thresholds. However, this also exposes issues stemming from the model's high sensitivity: an excess of false positives and lower precision, causing the overall CSI curve to shift toward the lower-left corner. Zone III (South China) achieved the lowest optimal CSI score of 0.161, corresponding to a probability threshold of 42%. It also exhibited the lowest hit rate across all thresholds, indicating the most conservative thunderstorm forecasting approach among the three regions. The CSI curve's overall leftward shift similarly reflects the model's reduced prediction frequency in high-probability intervals.

 doi:10.20944/preprints202603.2018.v1

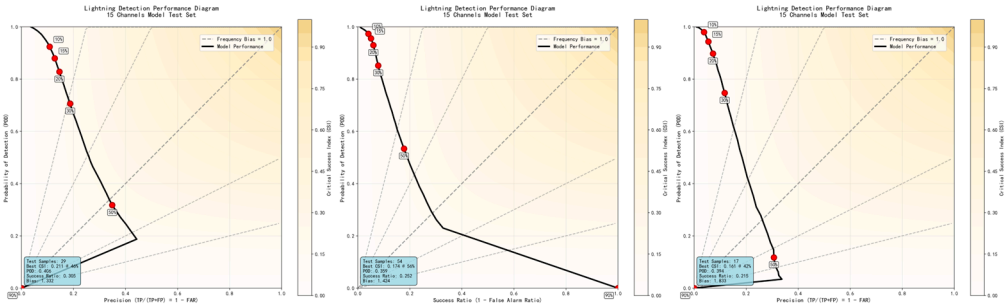

Figure 8. CSI performance diagrams of the AGToLightM model across the three study regions. From left to right: Zone I (East China), Zone II (North China), and Zone III (South China). The black curves represent the performance trajectories across various probability thresholds (10%–90%), while the background shaded contours indicate constant Critical Success Index (CSI) values.

Table 6. The optimal critical success index of the AGToLightM model and its corresponding probability threshold and accuracy performance.

Zone ID	Best probability threshold	CSI	POD	Precision
I	46%	0.211	40.6%	30.5%
II	56%	0.174	35.9%	76.2%
III	42%	0.161	39.4%	38.4%

The analysis of single forecasts across different regions and time periods reveals that model performance is closely correlated with lightning activity intensity. Forecast accuracy is significantly higher during periods of dense lightning activity compared to sparse activity, indicating the model excels at capturing lightning signals associated with strong convective events. Taking the Zone I (East China) as an example, representative time periods are selected for demonstration. Probability prediction results are shown in Table 7, where different probabilities are distinguished by contour lines and overlaid with actual lightning data (yellow markers). The corresponding CSI curves for each time period are also compared to analyze the comprehensive performance of the current forecast and evaluate prediction effectiveness. During periods of intense lightning activity (06:30-07:30 UTC, 07:30-08:30 UTC), the model demonstrated high hit rates and relatively stable CSI performance. Conversely, during periods of weaker lightning activity (e.g., 04:30-05:30 UTC, 05:30-06:30 UTC), forecast certainty decreased, leading to a corresponding decline in precision. The model demonstrates strong capability in capturing signals from severe convective lightning, but forecasting accuracy exhibits errors under conditions of weak or isolated lightning activity.

Table 7. Spatiotemporal evolution of thunderstorm probability forecasts and corresponding CSI performance curves for Zone I (East China) during representative intervals on August 25, 2025.

04:30-04:45 forecast **04:30-05:30** (UTC)	**05:30-05:45 forecast** **05:30-06:30** (UTC)	**06:30-06:45 forecast** **06:30-07:30** (UTC)	**07:30-07:45 forecast** **07:30-08:30** (UTC)
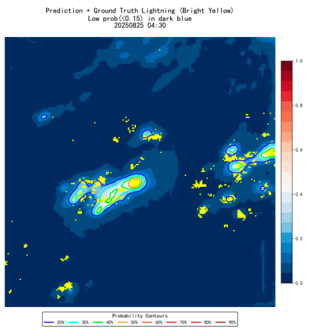	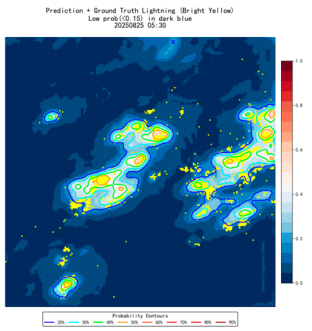	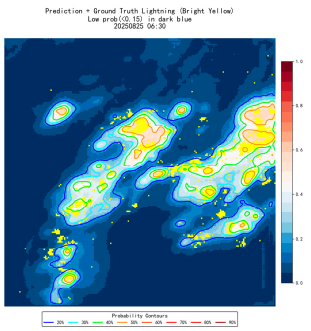	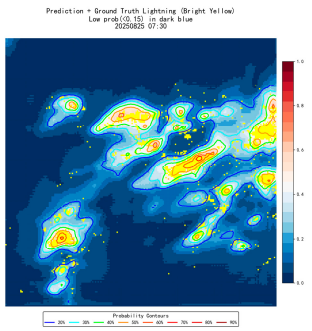

 doi:10.20944/preprints202603.2018.v1

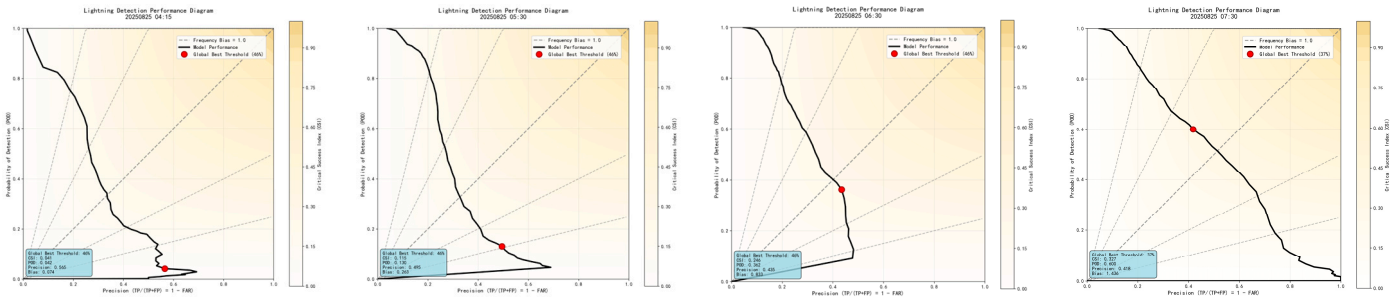

4.3. Analysis of the Influence of Feature Factors.

To analyze the influence of each feature factor on thunderstorm precursor signals, single-channel ablation tests were conducted for each feature factor. The results are shown in Figure 9 below.

The single feature factor ablation test results indicate that the omission of certain factors significantly impacts model performance. As shown in the figure, the TBDT (12.00–10.80) and TBDT (10.80–8.55) bands exert the greatest influence on model probability of detection (POD), reducing it by 16.7% and 8.3% respectively, while substantially enhancing model sensitivity. TBDT (10.80), BT(WV7.42), BT(IR8.55), and TBDT(12.00) also made corresponding positive contributions to POD. However, they also affected Precision, leading to false positives in the model. The three factors BTD(12.00-10.80), BTD(10.80-8.55), and BTD(6.25-7.42) exerted the strongest influence on Precision, reaching 18.6%, 13.1%, and 6.0% respectively, substantially reducing false alarm rates. For F1 and CSI scores, BTD(10.80-8.55), BTD(12.00-10.80), and BTD(6.25-7.42) hold the highest proportions, effectively enhancing the model's overall performance and directly improving the effectiveness of thunderstorm prediction. The BTD(12.00-10.80) factor demonstrated positive contributions across all four metrics, establishing itself as a critical model factor. Other factors, such as BT(WV6.95) and BT(IR13.3), contributed minimally to the model's overall performance. Overall, TBDT (12.00-10.80), TBDT (10.80-8.55), and BTD(6.25-7.42) substantially improve POD (reducing false negatives) but decrease F1 and CSI. BTD(10.80-8.55) and BTD(12.00-10.80) substantially reduce false positives and improve F1/CSI, but increase false negatives.

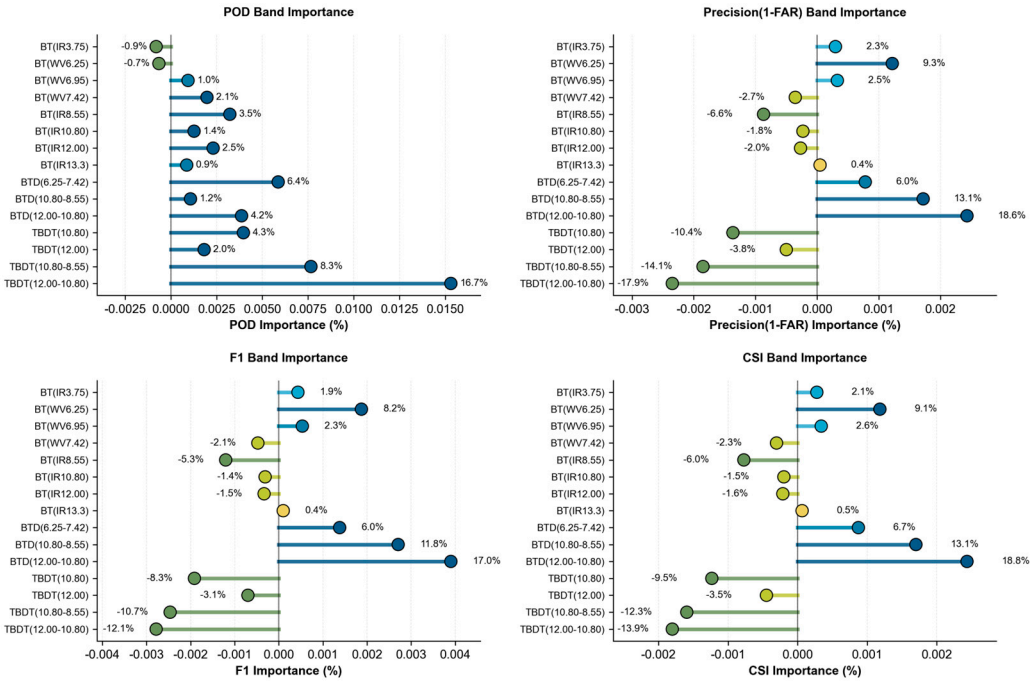

Figure 9. Importance analysis of feature factors. The bars indicate the percentage contribution of each satellite-derived feature to the POD, Precision, F1-score, and CSI metrics within the AGToLightM model.

 doi:10.20944/preprints202603.2018.v1

Analysis of comprehensive indicators reveals that the brightness temperature difference between 8.55 μm and 10.80 μm, as well as that between 12.00 μm and 10.80 μm, significantly impacts the model. Their temporal variations enhance the model's hit rate, while the current state substantially improves accuracy. During thunderstorms, intense convective updrafts cause rapid freezing of water vapor at the cloud top, forming numerous small ice particles (sleet, hail embryos, small snowflakes). Changes in cloud top temperature and particle characteristics can predict the future development trend of severe convection. The 8.55 μm channel exhibits strong scattering from small ice particles, resulting in relatively high radiative energy in convective regions and effectively reflecting convective conditions. Conversely, the 10.8μm band exhibits weak scattering/absorption by small ice particles. The brightness temperature difference between 8.55 μm and 10.80 μm shows significant variation within strong convective zones [53–55]. Studies indicate that BTD(10.80-8.55) yields positive values for ice clouds with high optical thickness and significantly negative values for water clouds with high optical thickness [42].

The absorption coefficients of water vapor and ice particles exhibit significant differences between 10.80 and 12.00 microns. The increase in water vapor's absorption coefficient between 10.80μm and 12.00 μm is substantially greater than that between 8.55 μm and 10.80 μm; conversely, ice's absorption coefficient changes in the opposite manner [56]. Consequently, ice particles significantly enhance radiation absorption in the 12.00 μm channel, while the 10.80 μm channel is less affected by ice particles, leading to a bright temperature difference. Strong convection, accompanied by intense vertical transport of water vapor, increases the water vapor content within the atmospheric column. This further enhances radiation absorption in the 12.00 μm channel, lowering BT(IR12.00) and making the BTD(12.00–10.80) more pronounced. Correspondingly, convective cells exhibit a distinct BTD(12.00–10.80), confirming the association between brightness temperature differences and areas of intense convective activity [57].

Secondly, the 6.25 μm and 7.42 μm channels, serving as water vapor absorption bands, exhibit channel differences that reflect the degree of anomaly in atmospheric vertical water vapor gradients, thereby contributing to improvements in model accuracy. The 6.25 μm channel is sensitive to water vapor in the upper-middle troposphere (300–500 hPa), while the 7.42 μm channel is more sensitive to water vapor in the lower-middle troposphere (500–700 hPa) Convective triggering theory indicates that when the upper atmosphere is dry and cold while the lower atmosphere is warm and moist, the atmosphere enters a conditionally unstable state. Once uplift triggers convection, it readily develops into severe convection. The difference between the 6.25 μm and 7.42 μm channels directly characterizes the vertical water vapor gradient, reflecting the degree of atmospheric instability in a "dry-wet" or "wet-dry" configuration. "dry-over-wet" or "wet-over-dry" instability [58], serving as a thermodynamic indicator of convective instability. The European Organisation for the Exploitation of Meteorological Satellites (EUMETSAT) and the China Meteorological Administration (CMA) have integrated BTD into their severe convection warning operational systems, enhancing warning lead times by 30–60 minutes [58].

4.4. Case Analysis

Based on the model, case analyses were conducted for the three regions. Figures 10–12 present the thunderstorm probability model results for these three areas.

On August 21, 2025, extensive short-duration heavy rainfall accompanied by thunderstorms and strong winds occurred across North China and East China. Figure 10 shows the thunderstorm forecast results for the North China region at four time intervals (05:00 UTC, 07:00 UTC, 09:00 UTC, 11:00 UTC) on August 21, 2025 UTC. Figure 10(a-d) uses different colors to indicate the probability of thunderstorm occurrence, with yellow pixels representing ground-based lightning measurement data. Figure 10(e-h) displays the composite reflectivity from weather radar at the forecast time.The color scale on the right represents the reflectivity intensity in dBZ, ranging from 0 to 70. The colored curves superimposed on these radar maps represent the probability contours output by the AGToLightM model. The figures reveal that at 05:00 UTC, precipitation was just beginning, with

 doi:10.20944/preprints202603.2018.v1

limited lightning activity and coverage. The forecast shows a small thunderstorm area and probability (maximum around 30%), consistent with the radar's high-echo zone. The model also predicted a 20% probability for the scattered lightning area in the lower right corner. As precipitation clouds intensified and shifted northward, two high-probability zones formed by 07:00 UTC in the northern and southwestern directions, both with forecast probabilities exceeding 50%. Notably, a 60% probability forecast emerged in the southwestern direction. This result shows high consistency with ground-based lightning and radar combined reflectivity data, particularly exhibiting significantly elevated probabilities in areas of dense lightning activity. By 09:00 UTC, convection intensified further, with the forecast density in the southwest direction increasing and the area with over 60% probability expanding. This high-probability zone aligned with the 50 dBZ radar reflectivity area at 09:00 UTC, indicating relatively heavy precipitation in that region. Meanwhile, the probability zones for thunderstorms in the northern and central parts of the map also expanded, largely aligning with the radar's high reflectivity areas. By 11:00 UTC, convection had developed into two distinct convective zones, north and south. The high-probability zone exceeding 60% coincided with both the ground-based lightning-dense area and the radar's 50 dBZ reflectivity zone, effectively predicting the occurrence of thunderstorms.

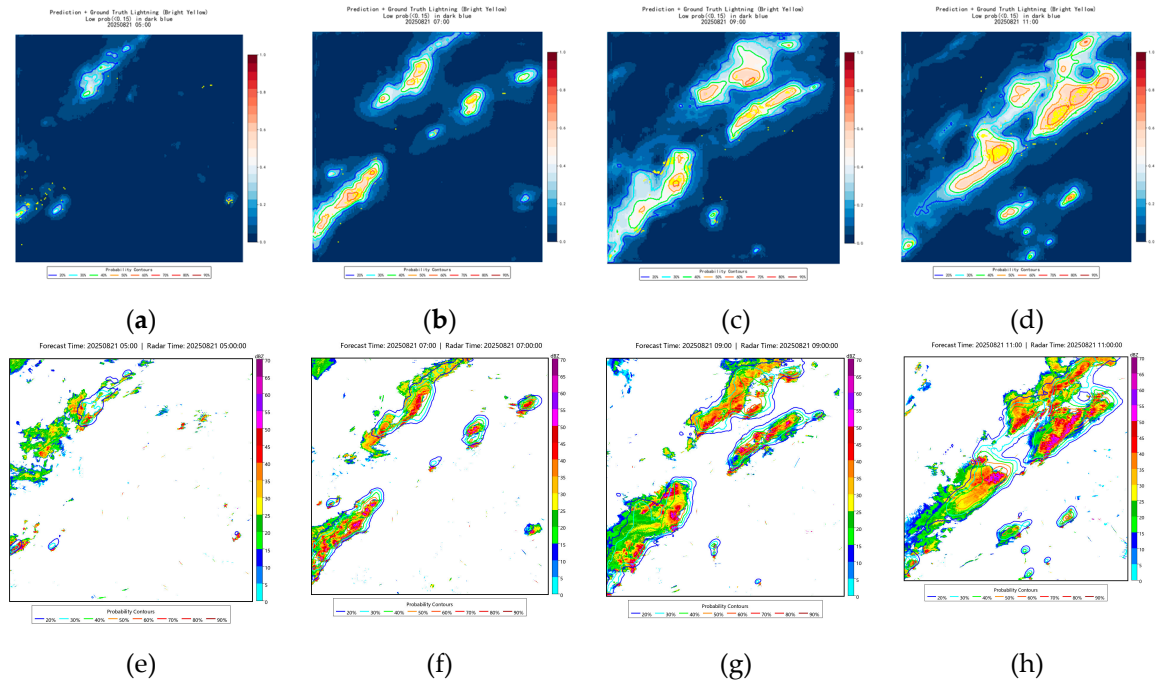

Figure 10. Comparison of Thunderstorm Forecast Results with Ground-Based Lightning and Weather Radar (20250821): (a) UTC 05:00 Thunderstorm Probability overlaid with Ground-Based Lightning; (b) UTC 05:00 Weather Radar Composite Reflectivity; (c) UTC 07:00 Thunderstorm Probability overlaid with Ground-Based Lightning; (d) UTC 07:00 weather radar composite reflectivity; (e) UTC 09:00 thunderstorm probability overlaid with ground-based lightning; (f) UTC 09:00 weather radar composite reflectivity; (j) UTC 11:00 thunderstorm probability overlaid with ground-based lightning; (h) UTC 11:00 weather radar composite reflectivity.

Figure 11 and Table 8 present the 15-minute forecast results and accuracy for the East China region on August 25, 2025. The figure shows that convective activity was highly active between 07:30 UTC and 08:00 UTC, with ground-based lightning observations recording over 1,800 strikes. Significant changes occurred within the 15-minute period, and the forecasted high-probability zones aligned with the areas of dense lightning distribution. The table summarizes the distribution of ground-based lightning observations across different probability zones and their accuracy. Results indicate that only 6% of lightning strikes occurred in low-probability zones (below 20%). These scattered strikes in low-probability areas may have been missed due to indistinct cloud features or misinterpreted lightning data. Over 50% of lightning strikes occurred in high-probability zones, as

 doi:10.20944/preprints202603.2018.v1

indicated by the red boundary area (50% probability line) in the figure. Their distribution overlapped with lightning-dense regions, effectively forecasting the location and area of thunderstorms.

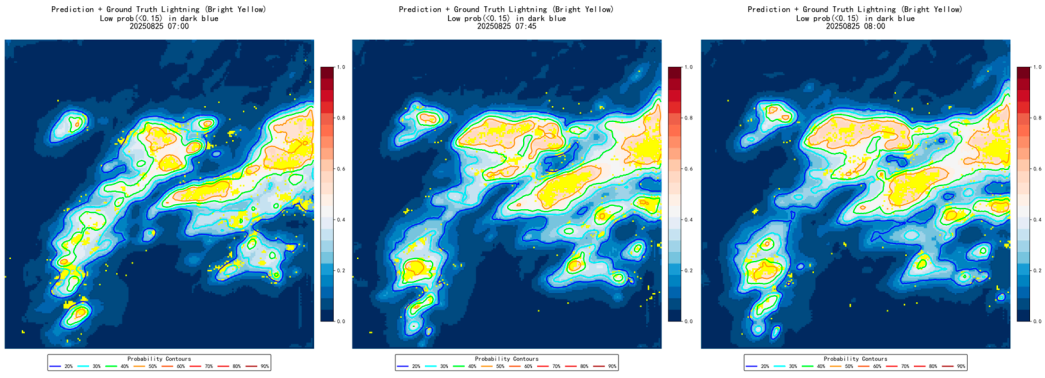

(a) (b) (c)

Figure 11. Spatiotemporal distribution of the 15-minute thunderstorm probability forecast for the East China region on August 25, 2025 (UTC).

Table 8. Quantitative verification of the East China regional forecast against ground-based lightning observations for the August 25, 2025 (UTC) event.

Time	Sample size(%)						POD(46%)	Precision
	<20	20-30	30-40	40-50	≥50	Total		
7:30	139	151	298	436	887	1911	56.9%	34.6%
7:45	100	160	271	438	886	1855	58.3%	38.4%
8:00	97	111	287	435	906	1836	59.9%	35.9%

Figure 12 illustrates the forecast results and corresponding accuracy for three consecutive periods in the South China region on August 27, 2025. A small-scale severe convective event occurred in this area between 09:00 and 12:00 UTC. As indicated in Table 9, the ground-observed lightning counts were significantly lower than those recorded during the East China event on August 25, 2025.

The predicted thunderstorm zones in Figure 12 largely overlap with the actual lightning occurrence areas, with probabilities exceeding 40% assigned to the relatively dense lightning clusters. During this period, fewer high-probability zones (> 50%) were produced, and some regions were slightly underestimated. Analysis suggests that the relatively weak convective intensity, coupled with modest brightness temperature differences and limited temporal variation rates, resulted in lower overall probability scores. This subdued intensity is further evidenced by the sparse ground-based lightning data. Despite the lower convective forcing, the model still accurately captured the radar-detected convective areas, demonstrating its reliability and robustness even under weak convective conditions.

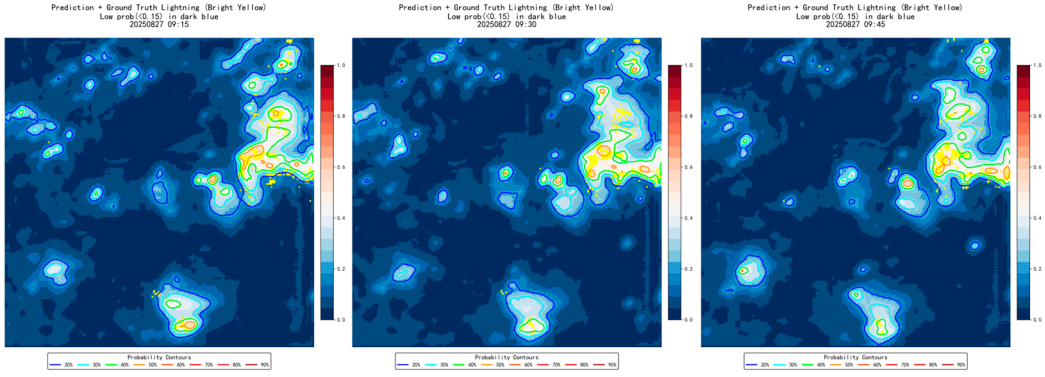

Figure 12. Performance of the thunderstorm probability model for the South China region across three consecutive intervals on August 27, 2025 (UTC).

 doi:10.20944/preprints202603.2018.v1

Table 9. Quantitative verification of the South China regional forecast against ground-based lightning observations for the August 27, 2025 event.

Time	Sample size(%)						POD(42%)	Precision
	<20	20-30	30-40	40-50	≥50	Total		
9:15	57	71	103	146	58	435	40.0%	22.7%
9:30	23	52	137	180	30	422	42.4%	21.9%
9:45	26	48	97	196	41	408	49.5%	27.5%

5. Conclusions

This study utilizes FY-4B/AGRI multi-channel infrared brightness temperature data and ground-based lightning observation records to construct AGToLightM, a 60-minute thunderstorm occurrence probability prediction model based on the Convolutional Block Attention Mechanism (CBAM) and an adaptive weighted loss function. Experimental validation was conducted across three typical thunderstorm-prone regions in North, East, and South China. The study also examined the differential contributions of various infrared channel features to thunderstorm identification and their radiative characteristics. Through a series of experiments and analyses, the following conclusions were drawn:

1. This model effectively predicts thunderstorm occurrence areas and probabilities within the next 60 minutes. Across all study zones, the average Critical Success Index (CSI) is 0.182, with a single-instance peak of 0.327. The average POD at the optimal CSI probability threshold is 39%, and the average precision is 48%. Areas with forecast probabilities exceeding 60% exhibit spatial consistency with regions featuring radar echoes above 50 dBZ.
2. The AGToLightM generates higher probability estimates in intense convective regions, aligning closely with high-density lightning clusters. While some underestimation persists in areas of sparse or weakening convective activity, the model remains reliable under varying convective forcing. Future iterations could integrate numerical weather prediction (NWP) data and multi-source sounding observations to further enhance model adaptability in complex meteorological environments.
3. Channel ablation experiments indicate that the channel brightness temperature difference in FY-4B/AGRI plays a dominant role in enhancing the model's overall performance, while the temporal brightness temperature difference requires trade-offs based on accuracy requirements.

References

1. Wang, Y.; Yussouf, N.; Mansell, E.R.; Matilla, B.C.; Kong, R.; Xue, M.; Chmielewski, V.C. Impact of Assimilating GOES-R Geostationary Lightning Mapper Flash Extent Density Data on Severe Convection Forecasts in a Warn-on-Forecast System. *Mon. Weather Rev.* **2021**, *149*, 3217–3241, doi:10.1175/mwr-d-20-0406.1.
2. Carey, L.D.; Rutledge, S.A. A Multiparameter Radar Case Study of the Microphysical and Kinematic Evolution of a Lightning Producing Storm. *Meteorol. Atmos. Phys.* **1996**, *59*, 33–64, doi:10.1007/BF01032000.
3. Deierling, W.; Petersen, W.A. Total Lightning Activity as an Indicator of Updraft Characteristics. *J. Geophys. Res.: Atmos.* **2008**, *113*, doi:10.1029/2007jd009598.
4. Fierro, A.O.; Gilmore, M.S.; Mansell, E.R.; Wicker, L.J.; Straka, J.M. Electrification and Lightning in an Idealized Boundary-Crossing Supercell Simulation of 2 June 1995*. *Mon. Weather Rev.* **2006**, *134*, 3149–3172, doi:10.1175/mwr3231.1.
5. Goodman, S.J.; Buechler, D.E.; Wright, P.D.; Rust, W.D. Lightning and Precipitation History of a Microburst-Producing Storm. *Geophys. Res. Lett.* **1988**, *15*, 1185–1188, doi:10.1029/GL015i011p01185.
6. MacGorman, D.R.; Burgess, D.W.; Mazur, V.; Rust, W.D.; Taylor, W.L.; Johnson, B.C. Lightning Rates Relative to Tornadic Storm Evolution on 22 May 1981. *J. Atmos. Sci.* **1989**, *46*, 221–251, doi:10.1175/1520-0469(1989)046%3C0221:lrrtts%3E2.0.co;2.

 doi:10.20944/preprints202603.2018.v1

7. Wiens, K.C.; Rutledge, S.A.; Tessendorf, S.A. The 29 June 2000 Supercell Observed during STEPS. Part II: Lightning and Charge Structure. *J. Atmos. Sci.* **2005**, *62*, 4151–4177, doi:10.1175/jas3615.1.
8. Fierro, A.O.; Mansell, E.R. Electrification and Lightning in Idealized Simulations of a Hurricane-like Vortex Subject to Wind Shear and Sea Surface Temperature Cooling. *J. Atmos. Sci.* **2017**, *74*, 2023–2041, doi:10.1175/jas-d-16-0270.1.
9. Fierro, A.O.; Mansell, E.R. Relationships between Electrification and Storm-Scale Properties Based on Idealized Simulations of an Intensifying Hurricane-like Vortex. *J. Atmos. Sci.* **2018**, *75*, 657–674, doi:10.1175/jas-d-17-0202.1.
10. Ávila, E.E.; Bürgesser, R.E.; Castellano, N.E.; Collier, A.B.; Compagnucci, R.H.; Hughes, A.R.W. Correlations between Deep Convection and Lightning Activity on a Global Scale. *J. Atmos. Sol. Terr. Phys.* **2010**, *72*, 1114–1121, doi:10.1016/j.jastp.2010.07.019.
11. J, G.S. *Predicting Thunderstorm Evolution Using Ground - Based Lightning Detection Networks.*; 1990;
12. ROY, S.S.; MOHAPATRA, M.; TYAGI, A.; BHOWMIK, S.K.R. A Review of Nowcasting of Convective Weather over the Indian Region. *Mausam* **2019**, *70*, 465–484.
13. K, V.Y.; Metzl C, B.T. Inferring Thunderstorm Occurrence from Vertical Profiles of Convection-Permitting Simulations: Physical Insights from a Physical Deep Learning Model. *Artificial Intelligence for the Earth Systems* **2025**, *4*.
14. Zhang Yijun; Hua Guiyi; Yan Muhong; An Xuemin The Correlation Analysis Of Electric Activity, Convection And Precipitation In Convective Cloud And Stratus. *Plateau Meteorology* **1995**, *14*, 13–22, doi:CNKI:SUN:GYQX.0.1995-04-001.
15. Zhang, X.; Sun, J.; Zheng, Y.; Zhang, Y.; Ma, R.; Yang, X.; Zhou, K.; Han, X. Progress in Severe Convective Weather Forecasting in China since the 1950s. Journal of Meteorological Research **2020**, *34*, 699–719.
16. Song, G.; Li, S.; Xing, J. Lightning Nowcasting with Aerosol-Informed Machine Learning and Satellite-Enriched Dataset. *npj Clim. Atmos. Sci.* **2023**, *6*, 126–10, doi:10.1038/s41612-023-00451-x.
17. Borque, P.; Vidal, L.; Rugna, M.; Lang, T.J.; Nicora, M.G. Distinctive Signals in 1-Min Observations of Overshooting Tops and Lightning Activity in a Severe Supercell Thunderstorm. *J. Geophys. Res.: Atmos.* **2020**, *125, e2020JD032856*.
18. Bourscheidt, V.; Ramos, M.-H. On the Use of Geostationary Lightning Mapper Data as a Proxy for Precipitation. *Preprint (SSRN)* **2023**, doi:10.2139/ssrn.4594358.
19. Erdmann, F.; Poelman, D.R. Insights into Thunderstorm Characteristics from Geostationary Lightning Jump and Dive Observations. *Nat. Hazards Earth Syst. Sci.* **2025**, *25*, 1751–1768, doi:10.5194/nhess-25-1751-2025.
20. Thiel, K.C.; Calhoun, K.M.; Reinhart, A.E.; MacGorman, D.R. GLM and ABI Characteristics of Severe and Convective Storms. *J. Geophys. Res.: Atmos.* **2020**, *125*, doi:10.1029/2020jd032858.
21. MURPHY, K.M.; CAREY, L.D.; SCHULTZ, C.J.; CURTIS, N.; CALHOUNe, K.M. Automated and Objective Thunderstorm Identification and Tracking Using Geostationary Lightning Mapper(GLM) Data. *J. Appl. Meteorol. Climatol.* **2024**, *63*, 47–64, doi:10.1175/JAMC-D-22-0143.1.
22. Cintineo, J.L.; Pavolonis, M.J.; Sieglaff, J.M. ProbSevere LightningCast: A Deep-Learning Model for Satellite-Based Lightning Nowcasting. *Weather Forecasting* **2022**, *37*, 1239–1257, doi:10.1175/WAF-D-22-0019.1.
23. Huaman Chinchay, J.H. Algorithm for Automatic Nowcasting Using ABI and GLM Data. In Proceedings of the AMS Annual Meeting; 2023.
24. Xia Jinyi; Guan Li The study on precipitation products corrected by optimal selection FY-4B AGRI channel based on random forest algorithm. *Torrential Rain and Disasters* **2024**, *43*, 598-606 (in Chinese), doi:10.12406/byzh.2023-194.
25. Zhang, M.; Lai, X.; Zhao, D.; Chen, L.; Cao, G.; Xu, N. Reconstruction of Hourly Sea Surface Temperature Based on FY-4B AGRI. *Int. J. Remote Sens.* **2025**, *46*, 6695–6710, doi:10.1080/01431161.2025.2541944.
26. Zhang Xiang Identification of strong convective clouds on FY-4B satellite based on Python language. *Wireless Internet Science and Technology* **2025**, *22*, 5-8 (in Chinese), doi:10.3969/j.issn.1672-6944.2025.03.003.
27. Zhang, J.; He, M. Methodology for Severe Convective Cloud Identification Using Lightweight Neural Network Model Ensembling. *Remote Sens.* **2024**, *16*, 2070, doi:10.3390/rs16122070.

 doi:10.20944/preprints202603.2018.v1

28. Wu, Q.; Shou, Y.-X.; Zheng, Y.-G.; Wu, F.; Wang, C.-Y. Detecting Hailstorms in China from FY-4A Satellite with an Ensemble Machine Learning Model. *Remote Sens.* **2024**, *16*, 3354, doi:10.3390/rs16183354.
29. Ren Suling; Zhao Wei; Cao Dongjie; Liu Ruixia Application of FY-4A daytime convective storm and lightning products in analyzing severe thunderstorm weather in North China. *Journal of marine meteorology* **2020**, *40*, 33–46, doi:10.19513/j.cnki.issn2096-3599.2020.01.004.
30. Yuan Tie; Qie Xiushu Spatial and Temporal Distributions of Lightning Activtities in China from Satellite Observation. *Plateau Meteorology* **2004**, 488–494, doi:CNKI:SUN:GYQX.0.2004-04-011.
31. Wang Jixin; Zhu Baoyou; Ma Ming Characteristics of lightning activity and its relationship with the atmospheric environment parameters in Southeast China. *Journal Of University Of Science And Technology Of China* **2017**, *47*, 403-412,434, doi:10.3969/j.issn.0253-2778.2017.05.005.
32. Li Jingxiao; Song Haiyan; Xiao Wenan; Du Xiaobing; Guo Fengxia Temporal-spatial characteristics of lightning over Beijing and its circumjacent regions. *Transactions of Atmospheric Sciences* **2013**, *36*, 235–245, doi:10.3969/j.issn.1674-7097.2013.02.012.
33. Zheng Dong; Meng Qing; Lv Weitao; Zhang Yijun; Ma Ming The Analysis of Spatial and Temporal Characteristic of Cloud-to-ground Lightning in Summer Around Beijing Areas. *JOURNAL OF APPLIED METEOROLOGY AND CLIMATOLOGY* **2005**, *16*, 638–644, doi:10.3969/j.issn.1001-7313.2005.05.010.
34. Yan Lincheng; Zhang Wenjuan; Zhang Yijun; Zhang Haizeng; Zheng Domng; Yao Wen; Sun Xiubin; Zhang Yixu Temporal and Spatial Distribution of Thunderstorms and Strong Winds with Characteristics of Lightning and Convective Activities in the South China Sea. *Journal of Applied Meteorology and Climatology* **2023**, *34*, 503–512, doi:10.11898/1001-7313.20230410.
35. Li Qingshen; Chen Yuhan; Zhang Yang; Lai Jinke; Liu Yinfeng; Pang Wenjing DDW1 Lightning Location System and Performance Evaluation. *Meteorological Science And Technology* **2020**, *48*, 788–794, doi:10.19517/j.1671-6345.20190526.
36. Li Yun; Qiu Shi; Sun Zheng; Liu Yicheng; Luo Xiaojun; Shi Lihua Detection Performance of FY-4A Lightning Mapping Imager Based on ADTD. *Journal of Army Engineering University of PLA* **2024**, *3*, 63–69, doi:10.12018/j.issn.2097-0730.20230801002.
37. Xu, M.; Qie, X.; Pang, W.; Shi, G.; Liang, L.; Sun, Z.; Yuan, S.; Zhu, K.; Zhao, P. Lightning Climatology across the Chinese Continent from 2010 to 2020. *Atmos. Res.* **2022**, *275*, 106251, doi:10.1016/j.atmosres.2022.106251.
38. Zhang, Y.; Zhang, Y.; Zou, M.; Wang, J.; Li, Y.; Tan, Y.; Feng, Y.; Zhang, H.; Zhu, S. Advances in Lightning Monitoring and Location Technology Research in China. *Remote Sens.* **2022**, *14*, 1293, doi:10.3390/rs14051293.
39. Zhang Daoyuan; Wang Meng; Shen Zhen; Wang Dapeng Data quality analysis and evaluation of DDW1 lightning locator. *Meteorological,Hydrological and Marine Instruments* **2024**, *41*, 13–16, doi:10.19441/j.cnki.issn1006-009x.2024.01.034.
40. Rui-xia, L.; Qi-feng, L.U.; Min, C.; Yong, Z.; Wen, H.; Xiao-qing, L.I. Quality Assessment of FY-4A Lightning Data in Inland China. *J. Trop. Meteorol.* **2020**, *26*, 286–299.
41. Lynn, B.; Yair, Y. Prediction of Lightning Flash Density with the WRF Model. *Adv. Geosci.* **2010**, *23*, 11–16, doi:10.5194/adgeo-23-11-2010.
42. Zhang, Y.; Stensrud, D.J.; Clothiaux, E.E. Benefits of the Advanced Baseline Imager (ABI) for Ensemble-Based Analysis and Prediction of Severe Thunderstorms. *Mon. Weather Rev.* **2021**, *149*, 313–332, doi:10.1175/mwr-d-20-0254.1.
43. Prata, A.J. Observations of Volcanic Ash Clouds in the 10-12 Mm Window Using AVHRR/2 Data. *Int. J. Remote Sens.* **1989**, *10*, 751–761, doi:10.1080/01431168908903916.
44. Henderson, D.S.; Otkin, J.A.; Mecikalski, J.R. Evaluating Convective Initiation in High-Resolution Numerical Weather Prediction Models Using GOES-16 Infrared Brightness Temperatures. *Mon. Weather Rev.* **2021**, *149*, 1153–1172, doi:10.1175/mwr-d-20-0272.1.
45. Zhen, Y.; Ming, L.; Xiaoda, L.; Jiayu, L. Analysis and Forecasting of Rainstorm Onset in Early Autumn 2024 in Chengdu. *Open Journal of Natural Science* **2025**, *13*, 789–798, doi:10.12677/ojns.2025.134083.
46. Mecikalski, J.R.; Bedka, K.M. Forecasting Convective Initiation by Monitoring the Evolution of Moving Cumulus in Daytime GOES Imagery. *Mon. Weather Rev.* **2006**, *134*, 49–78, doi:10.1175/mwr3062.1.

 doi:10.20944/preprints202603.2018.v1

47. Xue, Y.; Xu, M.; Li, J.; Li, B.; Min, M.; Zhang, P.; Yang, L. Geostationary Satellite–Based Proxy Radar Observations: Expanding Coverage for Storm Tracking. *Adv. Atmos. Sci.* **2025**, *43*, 307–320, doi:10.1007/s00376-025-5275-y.
48. Zhu, Q.; Li, H.; Sun, H.; Xia, T.; Wang, X.; Han, Z. 3DV-Unet: Eddy-Resolving Reconstruction of Three-Dimensional Upper-Ocean Physical Fields from Satellite Observations. *Remote Sens.* **2025**, *17*, 3394, doi:10.3390/rs17193394.
49. Lagerquist, R.; McGovern, A.; Homeyer, C.R.; II, D.J.G.; Smith, T. Deep Learning on Three-Dimensional Multiscale Data for next-Hour Tornado Prediction. *Mon. Weather Rev.* **2020**, *148*, 2837–2861, doi:10.1175/mwr-d-19-0372.1.
50. AnbuDevi, M.K.A.; Suganthi, K. Review of Semantic Segmentation of Medical Images Using Modified Architectures of UNET. *Diagnostics* **2022**, *12*, 3064, doi:10.3390/diagnostics12123064.
51. LEINONEN, J.; HAMANN, U.; GERMANN, U. Seamless Lightning Nowcasting with Recurrent-Convolutional Deep Learning. *ARTIFICIAL INTELLIGENCE FOR THE EARTH SYSTEMS* **2022**, *1*, 1–17.
52. Dong Tongtong Study on Lightning Strike Area Identification Based on Weather Radar Product Data-A Case Study of Ningbo and Its Surrounding Areas. phd Dong Tongtong-559, Nanjing University of Information Science & Technology: Nanjing, 2025.
53. Hu Yachao; Zhang Min; Huang Ziyu Identification Method and Flow of Convective Cloud Cluster Characteristic Parameters Based on Himawari8 Satellite Data , ***2024***.
54. Mecikalski, J.R.; Bedka, K.M.; Paech, S.J.; Litten, L.A. A Statistical Evaluation of GOES Cloud-Top Properties for Nowcasting Convective Initiation. *Mon. Weather Rev.* **2008**, *136*, 4899–4914, doi:10.1175/2008mwr2352.1.
55. Zhu Yaping; Cheng Zhoujie; Liu Jianwen Detection and Analysis on Deep Convective Clouds in a Frontal Cyclone Using Multispectral Remote Sensing Data. *JOURNAL OF APPLIED METEOROLOGY SCIENCE* **2009**, *20*, 428–436, doi:10.3969/j.issn.1001-7313.2009.04.006.
56. Strabala, K.I.; Ackerman, S.A.; Menzel, W.P. Cloud Properties Inferred from 8-12 Micron Data. *J. Appl. Meteorol. Climatol.* **1994**, *33*, 212–229, doi:10.1175/1520-0450(1994)033%3C0212:CPIFD%3E2.0.CO;2.
57. C, M.C.; S., A. Negative 11 Micron Minus 12 Micron Brightness Temperature Differences-A Second Look. In Proceedings of the 8th Conference on Satellite Meteorology and Oceanography; Atlanta, GA, 1996; pp. 313–316.
58. Santurette, P.; Georgiev, C.; Piriou, C. A DIAGNOSTIC TOOL BASED ON MSG 7.3μ/6.2μCHANNELS FOR THE ANALYSIS AND FORECASTING OF DEEP CONVECTION. In Proceedings of the 5th European Conference on Severe Storms; Landshut - GERMANY, 2009.